

## Effects of Minor Alloying Elements on the Metal-Dusting Behavior of Ni-Based Alloys

Bingtao Li  
High Temperature Corrosion Lab  
University of Pittsburgh  
Pittsburgh, PA  
USA

Wei-Ting Chen  
Missouri University of Science and  
Technology  
Rolla, MO  
USA

Brian Gleeson  
University of Pittsburgh  
Pittsburgh, PA  
USA

Heike Hattendorf  
VDM Metals International GmbH  
58762 Altena  
Germany

### ABSTRACT

Alloys are often found to suffer much greater metal-dusting attack under high-pressure conditions compared to ambient-pressure conditions. Ultimately, the resistance of a given alloy to metal dusting depends on the formation of an oxide scale that is impermeable to carbon which, in turn, depends on scale composition and structure. This paper reports the metal-dusting behavior of several Ni-based alloys having relatively high Cr contents (about 30 wt.%) and different controlled minor levels of Fe, Al, and/or Si. Testing was conducted under 20 bar total pressure of a high-carbon-activity gas at 600 °C (1112 °F). The exposed alloys were analyzed by SEM and TEM techniques to evaluate the oxide scales and evidence of carbon ingress. It was found that aluminum is beneficial to improve metal dusting resistance by reacting to form a continuous inner layer of alumina; whereas iron is detrimental to resistance. Mechanistic aspects of the role(s) played by minor elements in affecting metal-dusting resistance are considered.

Key words: Metal dusting, Ni-base alloys, Alloying elements, High-pressure testing, Chromia-scale, Alumina-scale

### INTRODUCTION

Metal dusting is a catastrophic form of corrosion that occurs when alloys are exposed at elevated temperature to a reducing environment with a very high carbon potential, such that the carbon activity,  $a_C$ , is greater than unity.<sup>1-6</sup> This form of corrosion is associated with carbon deposition

onto and penetration into the alloy, ultimately causing disintegration. The coke formation associated with carbon deposition also has the effect of reducing the heat-transfer efficiency of the alloy and, hence, service lifetime of the structure. Metallic materials are highly susceptible to metal dusting in the temperature range 400-800 °C (752-1472 °F), which is relevant to the operation of hydrogen, ammonia, and methanol plants. Within this temperature range the carbon activity can be high while the scaling kinetics, necessary for maintaining protection, are low.<sup>4</sup>

Many metallic materials are susceptible to metal dusting attack, including ferritic steels, alloy steels, stainless steels, Ni-base alloys, and Co-base alloys. Previous studies<sup>7-13</sup> on metal dusting mechanisms addressed the formation of cementite (Fe<sub>3</sub>C) and subsequent decomposition of the unstable cementite under a high  $a_C$  into graphite and iron particles for the case of Fe-base alloys; while Ni-based alloys follow a similar mechanism without forming the metastable intermediate M<sub>3</sub>C, but rather graphite grows directly into the oversaturated metal. In the case of Fe-base alloys, not only does iron dissolve carbon to form carbides, but it also acts as a catalyst for the formation of graphite to cause metal dusting.<sup>14,15</sup> Accordingly, iron can be very detrimental for metal dusting resistance, whether as a base metal or as a minor alloying constituent.

Carbon steel and low-alloy steels have low carbon solubility and relatively high carbon diffusivity because of their body-centered cubic (BCC) crystal structure, and thus, are highly susceptible to carbide formation.<sup>16</sup> On the other hand, austenitic stainless steels and Ni-based alloys have a face-centered cubic (FCC) base structure which has a low carbon diffusivity and relatively high carbon solubility, which combine to reduce the extent of carbide formation. In the case of iron-base alloys, the chromium diffusivity decreases with increasing nickel content and this can also detrimentally affect metal-dusting resistance.<sup>4,17</sup> Kloewer et al.<sup>18</sup> studied a large number of commercial alloys and found that the Fe-Ni-Cr alloys were much less resistant to metal dusting than Ni-base alloys.

Any resistance to metal dusting attack must come from the formation of a protective oxide scale. Specifically, the solubility of carbon in Cr<sub>2</sub>O<sub>3</sub> and Al<sub>2</sub>O<sub>3</sub> is very low and, as a result, a continuous scale of either oxide can have the ability to suppress carbon penetration to the alloy and subsequent metal dusting attack. For most commercial alloys, chromium is the major alloying element to form a Cr<sub>2</sub>O<sub>3</sub> scale for corrosion protection during service operation. A higher chromium content helps to form more protective Cr<sub>2</sub>O<sub>3</sub> scale.<sup>13</sup> In the study conducted by Kloewer et al.,<sup>18</sup> increase in chromium content significantly improved the metal-dusting resistance of Ni-base alloys. Both aluminum and silicon are effective alloying additions in improving the metal-dusting resistance.<sup>4,6</sup> In a study by Grabke et al.,<sup>7</sup> an Fe-18Cr-1Al-1Si alloy showed no metal dusting attack at ~1 bar pressure even though the chromium content is relatively low. The good metal dusting resistance in this case was deduced to be due to the presence of aluminum and silicon in the alloy. Copper as an alloying addition has also been found to impart metal dusting resistance because it does not form carbides and it is also non-catalytic to carbon deposition.<sup>19</sup>

This paper follows from a very recent paper by Hattendorf et al.<sup>20</sup> and studies in greater detail four Ni-base alloys from that study with controlled levels of minor alloying elements (Fe, Al, and Si), together with a baseline of 0.3 wt.% Mn. Of specific interest is to better understand the roles of these elements on dusting resistance under a high-pressure testing condition, which more closely reflects actual service conditions.

## EXPERIMENTS

The measured compositions of the four Ni-base alloys studied are presented in Table 1. All alloys contain a relatively high chromium content (29.7-30.4 wt.%) and can be defined as Cr<sub>2</sub>O<sub>3</sub>-scale formers. The alloy T21 is a commercial heat of Alloy 690 (UNS<sup>(1)</sup> N06690) and has a Cr content of 29.9 wt.% and a relatively high Fe content of 10.1 wt.%. The alloy T15 is a laboratory heat with lower Fe content (0.5 wt.%) in comparison with the alloy T21. The alloy T09 is a laboratory heat with high Al content (2.8 wt.%) and low Fe content (0.6 wt.%). The alloy T14 is a commercial heat of Alloy HT70 (UNS N06008) with high Si (1.2 wt.%) and low Al and Fe contents (0.1 wt.% and 0.5 wt.%, respectively). All heats were melted and secondary processed, including solution heat treated. The details of the alloy melting and processing can be found elsewhere.<sup>20</sup>

**Table 1**  
**Composition of the alloys studied in weight percent (wt.%)**

Alloy	C	Cr	Ni	Mn	Fe	Al	Si	Others <0.3
T21	0.02	29.9	58.9	0.3	10.1	0.2	0.3	Ti
T15	0.04	30.4	68.3	0.3	0.5	0.3	0.1	
T09	0.02	29.2	66.6	0.3	0.6	2.8	0.1	La
T14	0.03	29.7	68.0	0.3	0.5	0.1	1.2	Ce/La

Details of the experiment can be found in other papers.<sup>20-22</sup> Test coupons were 2 mm thick x 50 mm long x 10 mm wide in size, and all surface were ground to a 600-grit finish. The metal-dusting test was conducted in a 46%H<sub>2</sub>-37%CO-7%CO<sub>2</sub>-9%H<sub>2</sub>O (volume percent) gas mixture under 20 bar (290 psi) total pressure and 600 °C (1112 °F). The oxygen partial pressure of the testing gas was calculated to be 4x10<sup>-26</sup> bar, and the carbon activity was 163 based on CO reduction reaction, 452 based on Boudouard reaction, or 253 based on at water gas shift equilibrium. A given exposure duration was limited to one week because of coke formation on the testing fixture. Accordingly, the test was cycled every 125 hours, with the coupons cooled and cleaned in alcohol between cycles. The total exposure times were 4965 h for T21 and 5693 h for T15, T09, and T14.

After testing, the coupons were visually examined for any metal-dusting attack (e.g., pit formation), and then cross-sectioned for further characterization. The cross-sections were examined by scanning electron microscopy (SEM), and the oxide scales and internal carbides were examined in greater detail using both a transmission electron microscope (TEM) and a scanning transmission electron microscope - high angle annular dark field (STEM-HAADF). The compositions of the oxide scales were analyzed using energy dispersive X-ray spectroscopy (EDS).

---

<sup>(1)</sup> UNS Unified Numbering System for Metals and Alloys (UNS). UNS numbers are listed in Metals & Alloys in the Unified Numbering System, 10th ed. (Warrendale, PA: SAE International and West Conshohocken, PA: ASTM International, 2004).

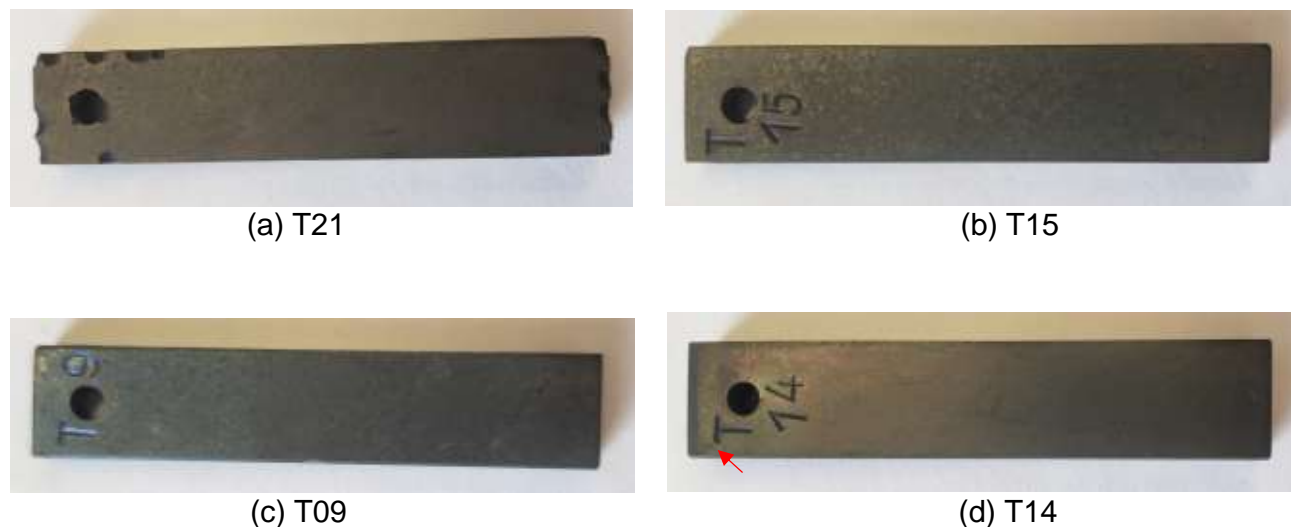
## EXPERIMENTAL RESULTS

Based on visual observation, the alloy T21 showed the first pit attack after 754 h exposure, and T14 showed a small pit after 1499 h exposure. The alloys T15 and T09 did not show any evidence of metal dusting attack after the entire exposure of 5693 h. Table 2 summarizes the results of alloy grain size, the time to form the first pit, and mass loss (after sample cleaning) for each alloy tested. It is seen that T21 and T14 had a comparable grain size of about 90  $\mu\text{m}$ , while T15 and T09 had larger grain sizes of 207  $\mu\text{m}$  and 162  $\mu\text{m}$ , respectively. It is also seen that T21 recorded large mass loss of 14.5  $\text{mg}/\text{cm}^2$ , which is consistent with its early pit formation. The other alloys exhibited negligible or no measurable mass loss.

**Table 2**  
**Observations and measurements of the tested alloys**

Alloy	Grain size, $\mu\text{m}$	Total exposure time, hours	Time for first pit to appear, hours	Mass loss, $\text{mg}/\text{cm}^2$
T21	96	4965	754	14.5
T15	207	5693	None	0.0
T09	162	5693	None	0.3
T14	89	5693	1499	0.0

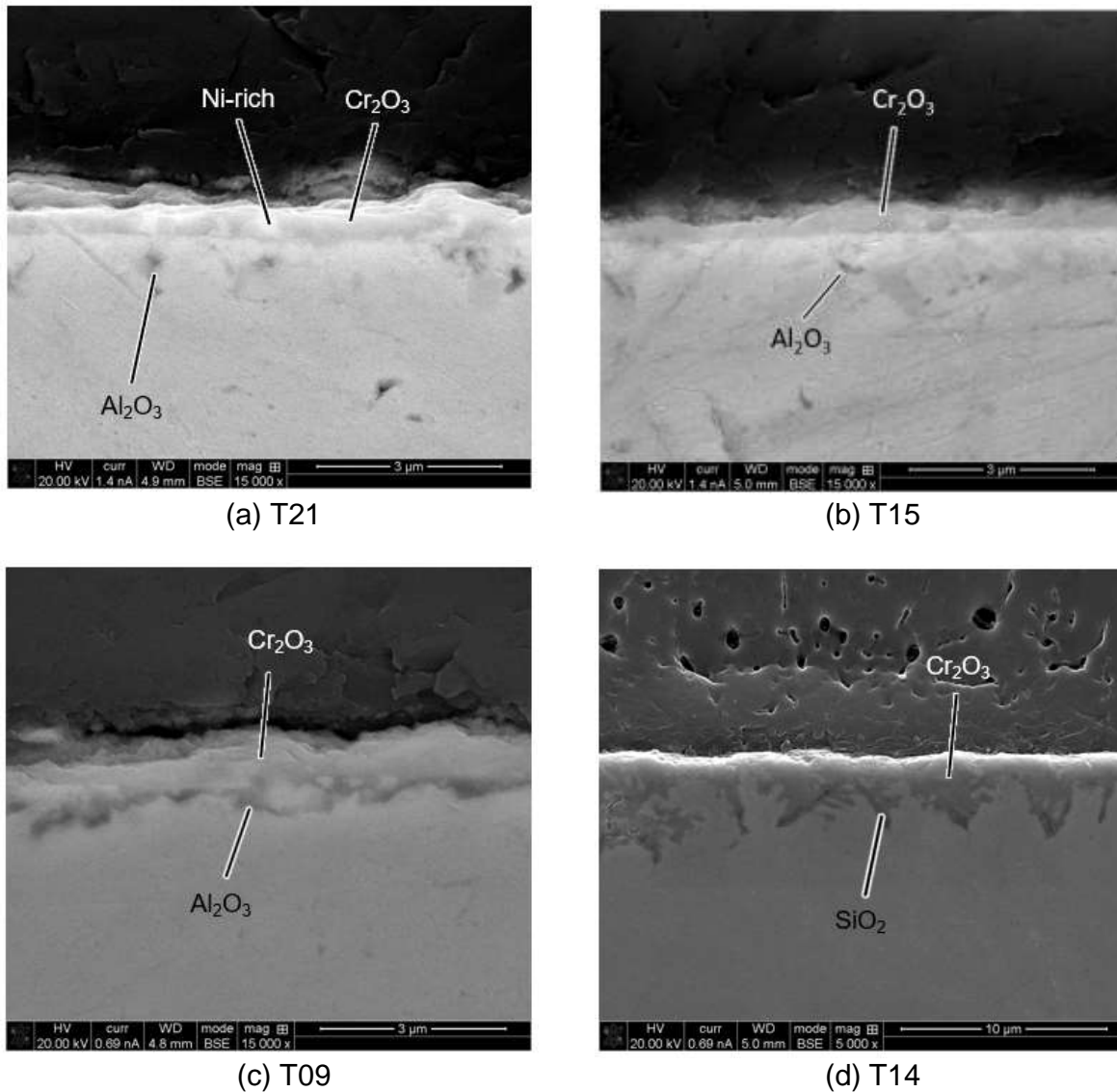
Figure 1 shows macro-images of the alloy coupons after total exposure. It is seen that the alloys T15 and T09 did not exhibit pit attack after the 5693 h of exposure. The pits on T21 were large and located along the edges of the coupon, including the edge of the drill hole. It was observed in Alloy T14 that the first pit (indicated by a red arrow) appeared after 1499 h exposure, but the pit size was small (less than 1mm) and did not show large growth after its appearance, which accounts for the non-measurable mass loss from this alloy (Table 2).



**Figure 1: Appearance of the alloy coupons after total testing exposure.**

Cross-sections of the exposed coupons were firstly examined using SEM/EDS, and representative images are presented in Fig. 2. All alloys formed an external chromia scale. Alloy T09 with 2.8 wt.% Al formed a continuous inner alumina layer, while internal Al-rich oxide was

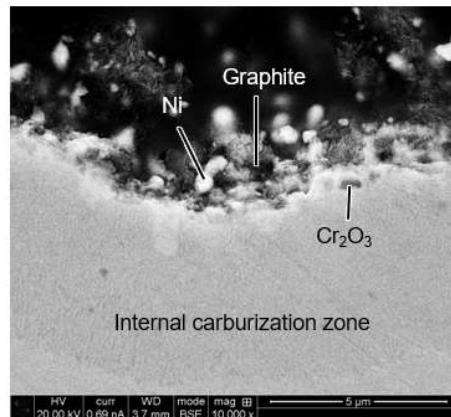
found in Alloys T21 and T15. Alloy T14 with 1.2 wt.% Si did not form a continuous inner silica layer, while large chromia protrusions formed, penetrating into the alloy matrix with silica precipitates at the protrusion front. On the basis of the EDS analyses, the chromia scales on all alloys contained a low level of manganese. Iron was also detected in the chromia scales, especially in the scale on Alloy T21. Different from the other alloys, localized Ni-rich particles were found in the chromia scale on T21. It is noted that the cross-sectional images in Fig.2 were all taken from areas free from pit attack and therefore represent areas that maintained good metal-dusting resistance. Accordingly, no internal carbides were observed in these cross-sections.



**Figure 2: Cross-sectional SEM images of the alloys studied (note: Mounting material above the oxide scales in the images).**

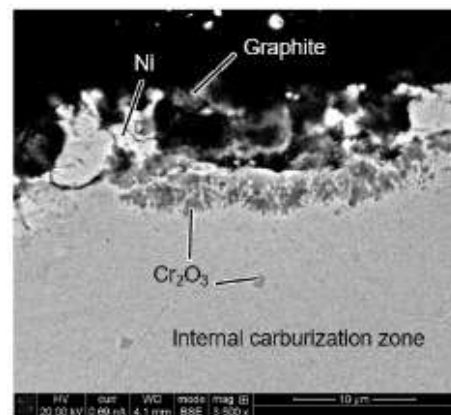
Figure 3 shows a cross-sectional SEM image at a metal dusting pit location in Alloy T21. The pit showed a typical metal dusting attack morphology, including graphite and Ni particles. In

addition, an internal carburization zone formed in the substrate region. The internal carbides were analyzed by STEM/EDS to be primarily  $\text{Cr}_3\text{C}_2$ .



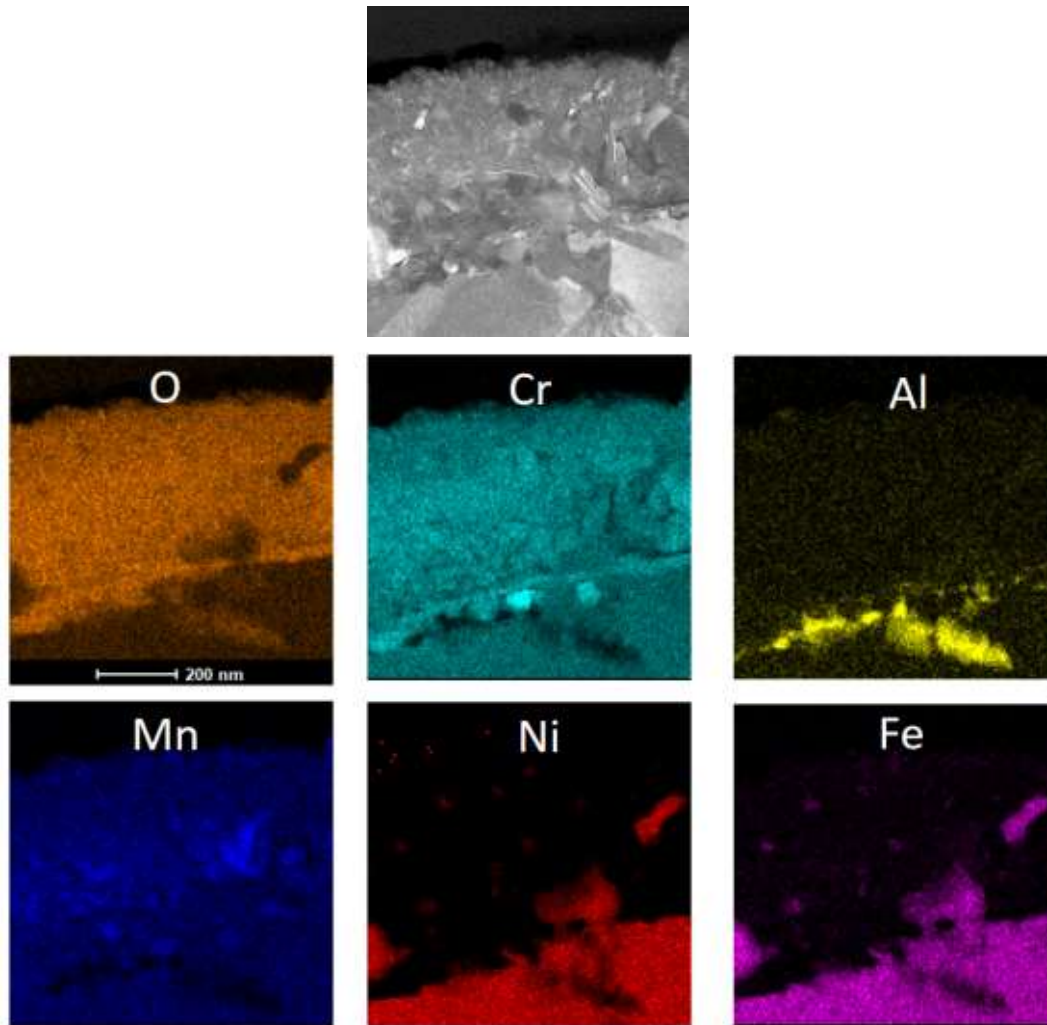
**Figure 3: Cross-sectional image at a metal dusting pit location in Alloy T21.**

Alloy T14 formed a few small pits after total exposure, and similar to T21, graphite and Ni particles were found in the pit, along with an internal carburization zone in the alloy substrate (Fig. 4). As indicated in Fig. 4, internal chromia formed in the surface region associated with the pit attack. Although the internal chromia did not provide metal dusting protection, it may have contributed to slow the pit growth in Alloy T14 (i.e., this alloy exhibited a slow progression of pit formation and growth).



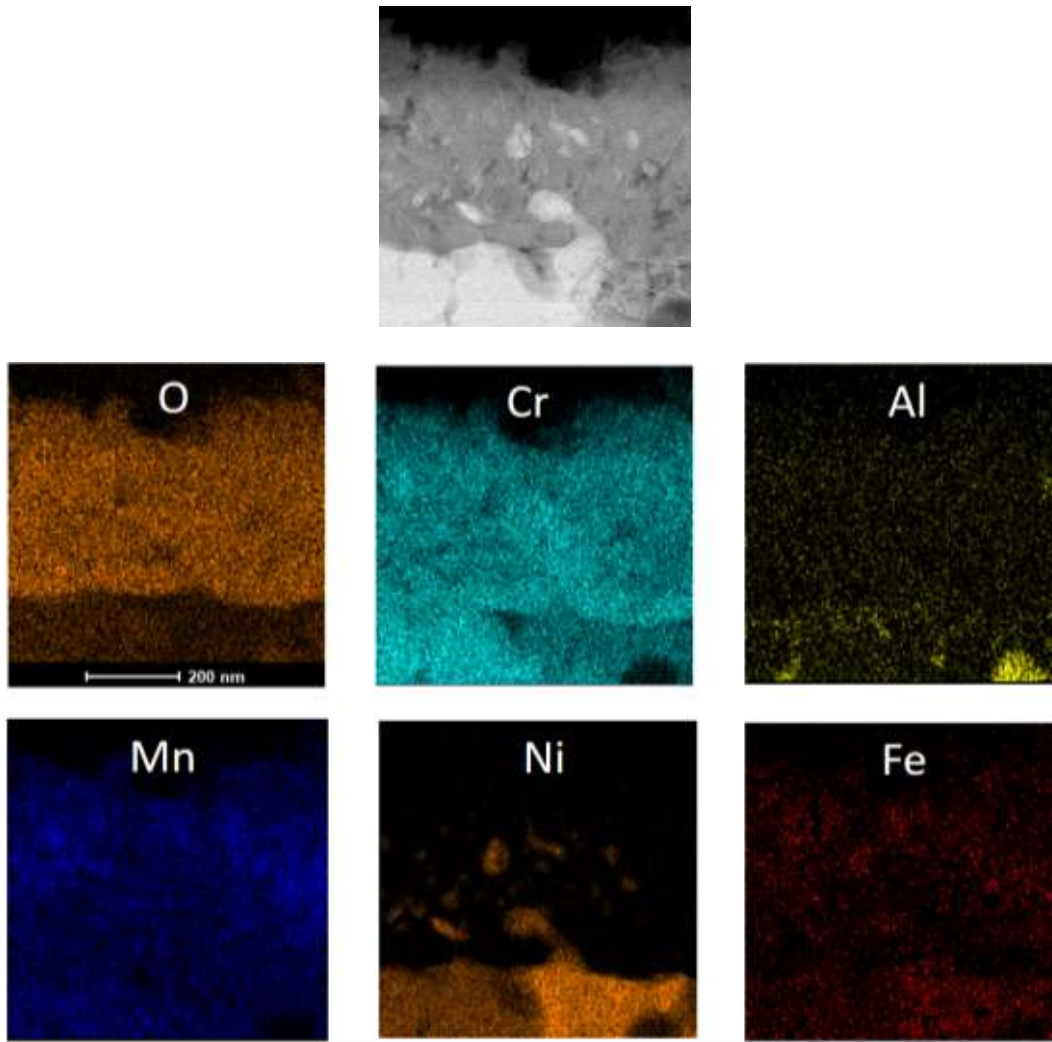
**Figure 4: Cross-sectional image at a metal dusting pit location in Alloy T14.**

The oxide scale that formed on Alloy T21 after total exposure was analyzed using the STEM (Fig. 5), and its thickness was measured to be about 400-500 nm. It is seen that the oxide scale had very fine and complicated structure. The STEM image is consistent with the SEM observation (Fig. 2) to the extent that an external chromia scale formed and alumina precipitated at the scale/substrate interface. Some metal particles rich in Ni and Fe were entrapped in the chromia scale. The area fraction entrapped metal particles was measured to be ~0.08. The collected EDS maps in Fig. 5 show Mn-rich oxide regions, which were deduced to be the spinel  $\text{MnCr}_2\text{O}_4$ .

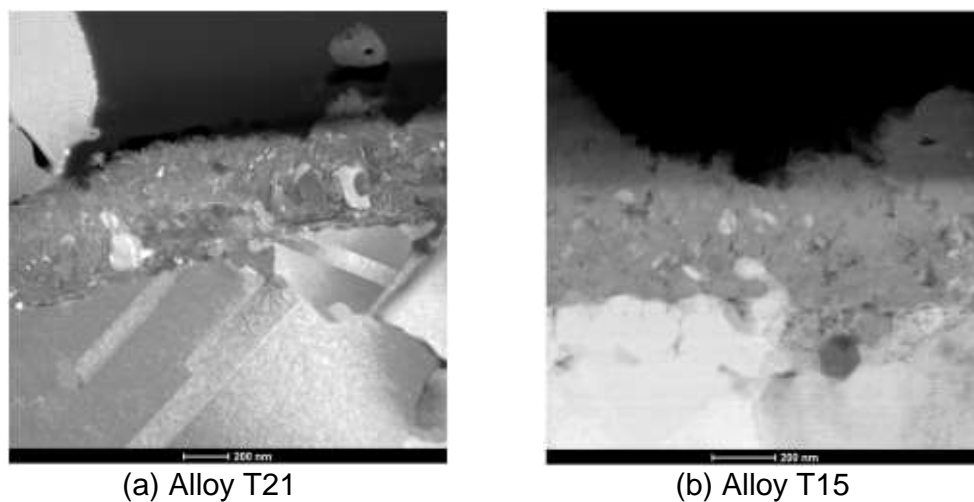


**Figure 5: TEM cross-section and associated EDS maps of oxide scale formed on Alloy T21 after total exposure.**

Similarly, the oxide scale formed on Alloy T15 after total exposure was examined and a representative TEM image is shown in Fig. 6. The oxide-scale thickness was measured to be about 450-700 nm. Compared with the results of Alloy T21 in Fig. 5, there was less amount of metal particles precipitated in the chromia scale and the metal particles were Ni-rich for Alloy 15 (i.e., no detectible Fe). The fraction of the metal particles was measured to be ~0.03 in the chromia scale formed on Alloy T15. Alumina precipitates were also detected at the scale/alloy interface. Figure 7 further compares the chromia scales formed on Alloys T21 and T15, and it clearly shows that the chromia scale formed on Alloy T15 was less heterogeneous than that formed on Alloy T21. Although Mn was detected in the chromia scale on Alloy T15, no  $\text{MnCr}_2\text{O}_4$  spinel was identified. This suggests that the Mn is in solid solution of the chromia scale on this alloy.

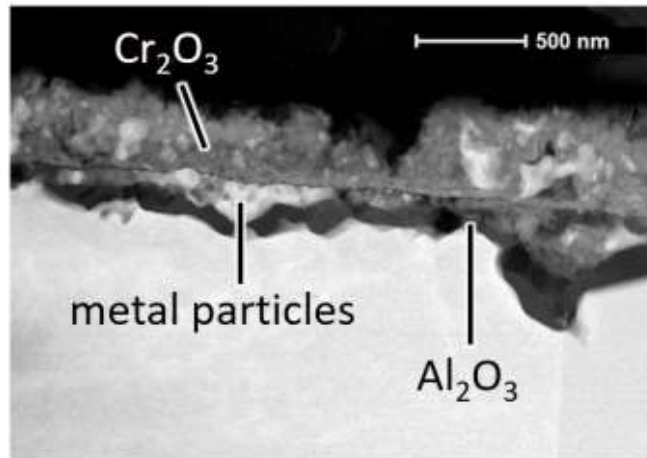


**Figure 6: TEM cross-section and associated EDS maps of oxide scale formed on Alloy T15 after total exposure.**



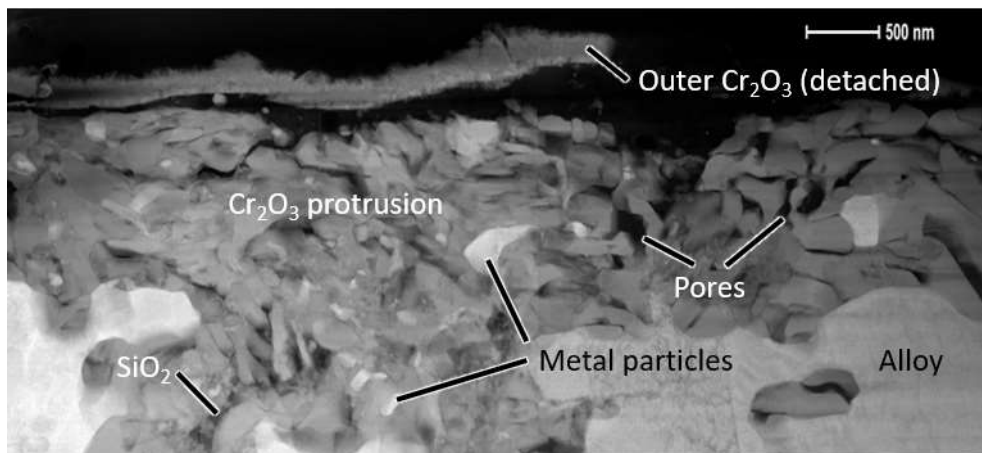
**Figure 7: Comparison of oxide scales formed on Alloys T21 and T15 after total exposure (the bright phases in the oxide scales are metal particles).**

A continuous inner alumina layer about 40-65 nm thick formed in the scale on Alloy T09 (Fig. 8). The external chromia layer was thinner, about 200-400 nm, when compared to those formed on Alloys T21 and T15. Further, a large number of Ni+Fe-enriched metal particles were entrapped within the chromia scale on Alloy T09. The area fraction of these metal particles was measured to be 0.13, which is much higher than what was measured in the chromia scales on Alloys T21 and T15. It is beyond that the scope of this study, but the high content of metal particles entrapped in the chromia scale formed on Alloy T09 may be due to growth stress and/or the mode of scale growth, which is influenced by minor constituents in the alloy.



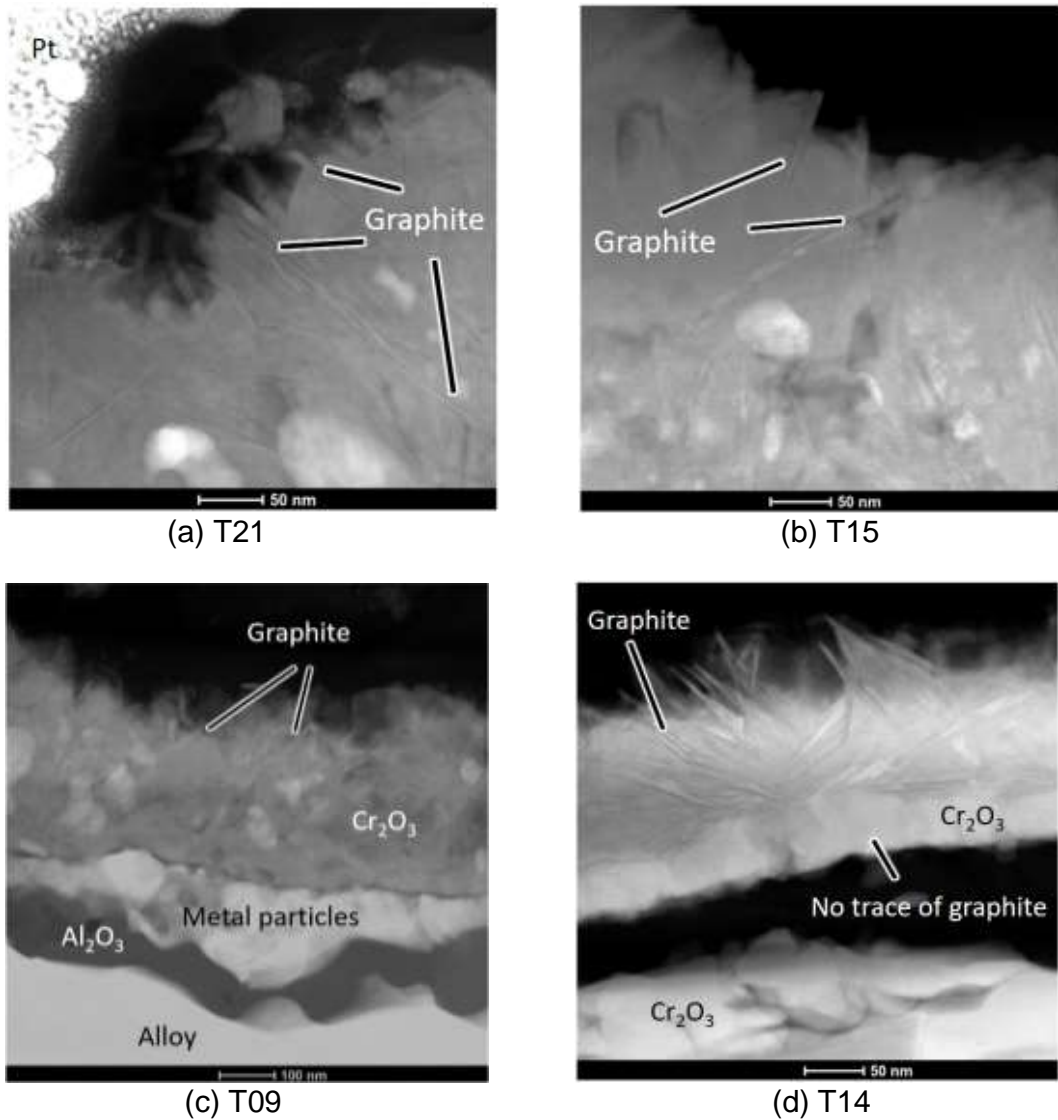
**Figure 8: Cross-sectional STEM-HAADF image of Alloy T09 after total exposure.**

Figure 9 shows the oxide scale formed on Alloy T14 examined using STEM-HAADF. The chromia scale thickness varied significantly due to its protrusion morphology, and silica precipitated at the protrusion front near scale/alloy interface. The chromia scale thickness without counting protrusion was about 150-200 nm. The chromia protrusions contained ~0.05 area fraction of metal particles, which is less than that in the other alloys. It is seen that the chromia scale exhibited a fragmented morphology, which is likely attributed to the formation of more voids or micro-channels. There was a thin and dense chromia layer at the surface of the scale, which was detached and possibly partially spalled. The amount of metal particles in this outermost chromia layer was significantly less than that in the thicker, underlying chromia layer.



**Figure 9: Cross-sectional STEM-HAADF image of Alloy T14 after total exposure.**

Another finding from the STEM examination was the precipitation of extensive graphite in the chromia scales formed on all alloys after the total exposure (Fig. 10). The graphite was very thin and acicular in morphology, with a length of up to a couple of hundred nanometers. This acicular graphite prevalently formed within the subsurface of the chromia scales, but also showed differences in formation behavior amongst the alloys studied. In the cases of Alloys T21 and T15 the graphite was found to exist through the entire chromia scales, with more in the outer portion and less in the inner portion next to the alloy substrate. By contrast, the graphite was only found in the outer portion of the chromia scale formed on Alloy T09, and no graphite was found in the inner alumina layer. For Alloy T14, graphite was only found in the dense outer chromia layer (e.g., the thin detached outermost layer in Fig. 9). In general, more graphite was found to form in Alloys T21 and T14 than in Alloys T15 and T09.



**Figure 10: STEM-HAADF images showing acicular graphite formation in the chromia scales formed on all alloys studied.**

The graphite formed in the detached thin chromia layer on Alloy T14 was further examined and an EDS line scan across the graphite penetrating into the chromia scale is shown in Fig. 11. A crack formed between the dense acicular graphite plates, suggesting that the plates can facilitate formation of short-circuit paths for carbon penetration. The EDS scan results showed enrichment of carbon, iron, and manganese at the graphite penetration location. The Mn and Fe contents in the chromia scales having graphite formation were analyzed by EDS for the four alloys studied, and the results are summarized in Table 3. It is seen that the Mn and Fe contents in T21 and T14 were significantly higher than that in T15 and T09. These former alloys, which were also the only ones to exhibit pit formation, also showed the greatest amount of graphite formation (i.e., through the scales).

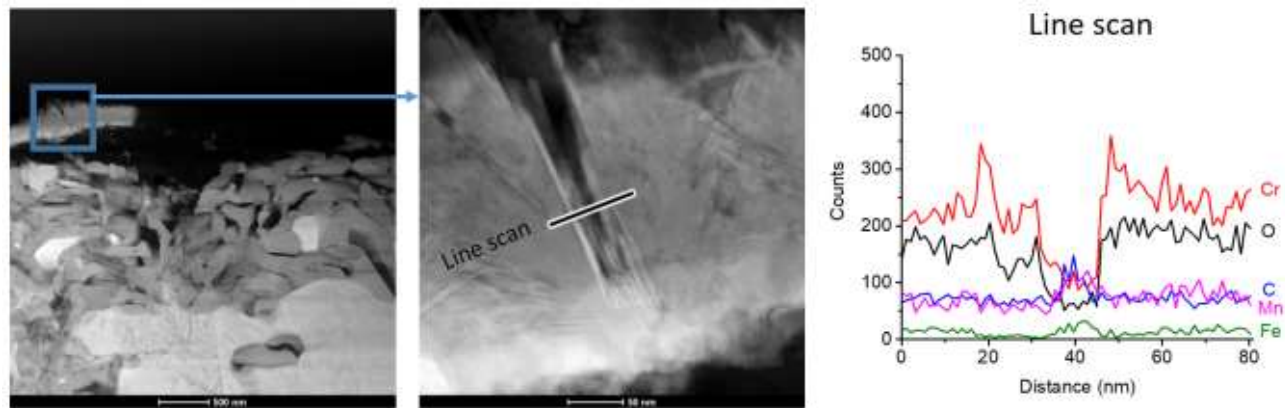


**Figure 11: EDX line scan across the crack and graphite which penetrated into the thin chromia layer at the surface of the oxide scale formed on Alloy T14.**

**Table 3**  
**Mn and Fe contents (wt.%/at.%) in the chromia layer with graphite formation**

Alloy	Mn	Fe	Mn+Fe
T21	6.9/4.6	3.0/1.9	9.9/6.5
T15	4.9/3.2	0.7/0.4	5.6/3.6
T09	3.4/2.1	1.4/0.9	4.8/3.0
T14	7.7/4.8	3.4/2.1	11.1/6.9

## DISCUSSION

Four Ni-base alloys containing similar chromium contents, i.e. 29.7-30.4 wt.%, with different minor alloying elements, i.e. 0.5-10.1 wt.% Fe, 2.8 wt.% Al, or 1.2 wt.% Si, were tested at 600 °C (1112 °F) under metal-dusting conditions at 20 bar pressure. The test gas composition was 46% $H_2$ -37% $CO$ -7% $CO_2$ -9% $H_2O$  with a low oxygen partial pressure of  $4 \times 10^{-26}$  bar and a carbon activity of 452 based on the Boudouard reaction. The testing was cyclic, with each cycle about 125 h and the total test time being up to 5693 h. Two alloys, T15 (30.4Cr-0.5Fe) and T09 (29.9Cr-2.8Al-0.6Fe), showed excellent metal-dusting resistance, with no observable pit initiation and with very low or immeasurable weight change after the total exposure. Alloy T21 (29.9Cr-10.1Fe) showed the worst metal-dusting resistance, with the first appearance of pits after 754 h exposure and extensive internal carburization. Alloy T14 (29.7Cr-1.2Si-0.5Fe) showed better metal-dusting resistance than T21 (29.9Cr-10.1Fe), with the first pit appearing

after 1499 h of exposure. The pits in T14 were much smaller and their growth was slow, which implies that it had better dusting resistance than T21. The better performance of T15 (30.4Cr-0.5Fe) compared to T14 (29.7Cr-1.2Si-0.5Fe) reveals that the addition of 1.2 wt.% Si is not essential for the design of metal-dusting-resistant alloys. The pits that formed on T21 and T14 were mainly located on edge locations, with the flat regions of the test coupons showing good metal-dusting resistance. This suggests that the chromia scales that formed on T21 and T14 are protective in the absence of defects (i.e., formation of defects tends to be promoted at sample edges), which is not realistic from a practical standpoint. The susceptibility of the chromia scales formed on these alloys to breaking down against dusting attack seemed to correlate with their extent of acicular graphite formation and amount of entrapped metal particles. The reasons for the observed variations in acicular graphite formation and of entrapped metal particles are still not fully understood.

Based on the SEM and TEM examinations, it was verified that all the alloys studied formed a chromia-rich scale. However, there were differences. For T21 and T15, which were without Al or Si additions, their scales were primarily chromia, but the high-Fe-containing T21 – the poorest performing alloy – also contained  $\text{MnCr}_2\text{O}_4$  spinel together with a high Fe content in the scale. Comparison between T21 and T15 suggests that, in the absence of further alloying additions, dusting resistance may be provided by the  $\text{Cr}_2\text{O}_3$  scale if the Fe content in the alloy is kept very low (i.e., below about 0.5 wt.%). Significantly, it is inferred that incorporation of Fe into a  $\text{Cr}_2\text{O}_3$  scale is detrimental to the scale providing dusting resistance. This is at least partly supported by the results of Nguyen et al.<sup>23</sup>, who reported carbon penetration through  $\text{Cr}_2\text{O}_3$  scales formed on Fe-20Cr initially exposed to Ar-20O<sub>2</sub> and then to Ar-20CO<sub>2</sub> at 650 °C. Atom probe maps presented in that study clearly showed a correlation between Fe and C distributions in the scale. Indeed, it is well established that Fe is a strong carbide former and acts as a catalyst for the carbon-deposition process, which is detrimental to metal dusting resistance.<sup>24</sup>

Alumina and silica are more stable than chromia and are therefore able to form beneath a chromia scale, near to the alloy. The relatively high Al content (2.8 wt.%) in T09 enabled the formation of a continuous inner alumina layer which, in turn, imparted excellent dusting resistance to this alloy. In other words, it is inferred that the excellent dusting resistance found with Alloy T09 was due to the presence of an inner alumina layer in the scale. Alumina seems to be much more resistant to carbon penetration than chromia. The T14 alloy with a Si content of 1.2 wt.%, did not form a protective inner silica layer. Instead, silica was found to precipitate mostly on the front of the chromia protrusions in T14. The Si content of 1.2 wt.% seems to be too low for the alloy composition and conditions tested to be beneficial by reacting to form a continuous inner silica layer.

Acicular graphite with lengths up to 200 nm was found to form in the chromia scales. There was no consistent orientation relation between the graphite and the chromia matrix. Cracks were found to accompany with the formation of graphite in T14, which could promote scale failure. It is postulated that the presence of acicular graphite in a chromia scale could not only provide a short-circuit diffusion path for carbon penetration, but perhaps more detrimentally, the graphite could promote cracking within the chromia scale. The location of acicular graphite formation was detected to have higher Mn and Fe levels, which indicates the catalytic effect of Mn and Fe for carbon crystallization in the chromia scale. It is noted that the alumina layer formed did not contain graphite. Based on the results, it is concluded that chromia is more favorable for graphite formation than alumina, and the formation of graphite is detrimental for chromia scale to provide long-term metal dusting resistance.

## CONCLUSIONS

Metal-dusting exposures were conducted on four Ni-base alloys with different minor alloying elements under 20 bar pressure at 600 °C (1112 °F). The four alloys contained a similar, high level of Cr (29.7-30.4 wt.%), but included different Fe, Al, or Si contents. The alloys with a low Fe content (T15, 30.4Cr-0.5Fe) and high Al content (T09, 29.9Cr-2.8Al-0.6Fe) exhibited the best dusting resistance, with no evidence of pit formation and with negligible mass change. The alloy with a high Fe content (T21, 29.9Cr-10.1Fe) experienced the most severe metal dusting attack, with pits appearing after 754 h exposure and extensive internal carburization. The high Si content of the T14 (29.7Cr-1.2Si-0.5Fe) alloy showed better metal dusting resistant behavior with the formation of few small pits than T21.

Chromia scales formed on the alloys studied and included metal particles enriched with Ni and Fe, along with voids. Alloy T15, with the least amount of metal particles in its chromia scale, showed excellent metal-dusting resistance. Mn and Fe were detected in the chromia scales on all alloys, and T21 and T14 containing higher Mn and Fe contents, i.e. 6.6 at.% and more, showed worse metal dusting resistance when compared with T15 and T09 with lower Mn and Fe contents (<3 at.%) in their chromia scales. The combination of the high fraction of metal particles and high Mn and Fe contents in the chromia scale is believed to cause the early breakdown of the chromia scale at the edges of the T21 and T14 coupons. Alloy T09 with 2.8 wt.% Al addition formed a continuous and dense inner alumina layer, which provided excellent metal dusting resistance. Addition of 1.2 wt.% Si in T14 did not show a beneficial effect in improving metal dusting resistance when compared with T15 having similar Cr and Fe levels, but low Si content. Thus, a Si addition of 1.2 wt.% is not essential to the design of a dusting-resistant alloy.

Acicular graphite formed and penetrated into the chromia scales on all four alloys studied. The existence of Mn and Fe in the chromia scales were likely associated with the formation of the acicular graphite. Cracks accompanied with the formation of acicular graphite in the chromia scale, which could decrease the resistance of the chromia scale to metal dusting attack. No graphite was found to form in the inner alumina layer on Alloy T09. The results of this study show clear evidence of the superiority of alumina in resisting both carbon ingress towards the underlying alloy and breakdown to metal dusting attack.

## REFERENCES

1. F.A. Prange, *Corrosion*, 12 (1959) 13.
2. W.B. Hoyt and R.H. Caughey, *Corrosion*, 12 (1959) 21.
3. H. Stahl and S.G. Thomsen, "Survey of worldwide experience with metal dusting", Ammonia Technical Manual. 36 (1996) 180.
4. G. Y. Lai, "High-Temperature Corrosion and Materials Applications", ASM International, (2007): p.97.
5. S.L. Britton and G.A. Cooper, "New Trends in Alloy Resistance to Metal Dusting in High Steam, Low Temperature Syngas", *Corrosion 2015*, NACE International, Paper 5614, (2015).

6. H. Hattendorf, A. Lopez, and J. Kloewer, "Alloy 699XA - New Alloy for Application under Metal Dusting Conditions", *Corrosion* 2018, Paper 11200, NACE International, (2018).
7. H.J. Grabke, R. Krajak, E.M. Muller-Lorenz, *Werkst. Korros.*, 44 (1993) 89.
8. H.J. Grabke, *Materials and Corrosion*, 54 (2003) 736.
9. H.J. Grabke, R. Krajak, E.M. Muller-Lorenz, and S. Straub, *Mater. Corros.*, 47 (1996) 495.
10. D.J. Young, J. Zhang, C. Geers and M. Schütze, *Mater. Corros.*, 62 (2011) 7.
11. R.F. Hochman, in: Proceedings of the Materials Engineering and Sciences Division Biennial Conference, AIChE 1970, Session No. 48, (1970): p. 401.
12. H.J. Grabke, R. Krajak, J.C. Nava Paz, *Corros. Sci.*, 35 (1993) 1141.
13. H.J. Grabke, *Mater. Corros.*, 49 (1998) 303.
14. F. Eberle and R. D. Wylie, *Corrosion*, 15 (1959) 622.
15. R. F. Hochman, Electrochemical Society Inc. Proc. 1976, 77-1 (1986): p.715 – 732.
16. B.A. Baker and G.D. Smith, "Alloy Selection for Environments Which Promotes Metal Dusting", NACE 2000, Paper No. 257, (2000).
17. H. J. Grabke, U. Gravenhorst, and W. Steinkusch, *Werkst. Korros.*, 27 (1976) 291.
18. J. Kloewer, H.J. Grabke, E.M. Muller-Lorenz, and D.C. Agarwal, "Metal Dusting and Carburization Resistance of Nickel-Base Alloys", Paper No. 139, *Corrosion/97*, NACE International, (1997).
19. David J. Yang and Jianqiang Zhang, *ECS Transactions*, 16(44) (2009) 3-15.
20. Heike Hattendorf, Chrétien G.M. Hermse, and Richard M. IJzerman, *Mater. Corros.*, 70 (2019) 1385.
21. C. Hermse and J.C. van Wortel, *Corros. Engin. Sci. Tech.*, 44 (2009) 182.
22. C. Hermse, A. Kempen, H. van Wortel, "Metal Dusting: What Determines Aggressivity?", Paper 07416, *Corrosion 2007*, NACE, Houston, TX, (2007).
23. T.D. Nguyen, A. La Fontaine, L. Yang, J.M. Cairney, J. Zhang, and D.J. Young, *Corros. Sci.*, 132 (2018) 125.
24. K. Natesan and Z. Zeng, "Development of Materials Resistant to Metal Dusting Degradation", Report ANL-07/30, Argonne National Laboratory, (2007).